Defence Technology 40 (2024) 78–90

Contents lists available at ScienceDirect

Defence Technology

journal homepage: www.keaipublishing.com/en/journals/defence-technology

A data and physical model dual-driven based trajectory estimator for long-term navigation

Tao Feng [a], Yu Liu [a, c], Yue Yu [b, d, *], Liang Chen [d], Ruizhi Chen [d]

[a] School of Communications and Information Engineering, Chongqing University of Posts and Telecommunications, Chongqing, 400065, China
[b] Department of Land Surveying and Geo-Informatics, The Hong Kong Polytechnic University, Hong Kong, 999077, China
[c] Chongqing Key Laboratory of Autonomous Navigation and Microsystem, Chongqing University of Post and Telecommunications, Chongqing, 400065, China
[d] State Key Laboratory of Information Engineering in Surveying, Mapping and Remote Sensing (LIESMARS), Wuhan University, Wuhan, 430000, China

ARTICLE INFO

Article history:
Received 15 January 2024
Received in revised form
13 April 2024
Accepted 14 May 2024
Available online 15 May 2024

Keywords:
Long-term navigation
Wearable inertial sensors
Bi-LSTM
QSMF
Data and physical model dual-driven

ABSTRACT

Long-term navigation ability based on consumer-level wearable inertial sensors plays an essential role towards various emerging fields, for instance, smart healthcare, emergency rescue, soldier positioning et al. The performance of existing long-term navigation algorithm is limited by the cumulative error of inertial sensors, disturbed local magnetic field, and complex motion modes of the pedestrian. This paper develops a robust data and physical model dual-driven based trajectory estimation (DPDD-TE) framework, which can be applied for long-term navigation tasks. A Bi-directional Long Short-Term Memory (Bi-LSTM) based quasi-static magnetic field (QSMF) detection algorithm is developed for extracting useful magnetic observation for heading calibration, and another Bi-LSTM is adopted for walking speed estimation by considering hybrid human motion information under a specific time period. In addition, a data and physical model dual-driven based multi-source fusion model is proposed to integrate basic INS mechanization and multi-level constraint and observations for maintaining accuracy under long-term navigation tasks, and enhanced by the magnetic and trajectory features assisted loop detection algorithm. Real-world experiments indicate that the proposed DPDD-TE outperforms than existing algorithms, and final estimated heading and positioning accuracy indexes reaches 5° and less than 2 m under the time period of 30 min, respectively.

1. Introduction

The ability to provide stable and enduring indoor localization is rapidly becoming a paramount requisite for indoor location-based services (iLBSs). Meticulous documentation of urban pedestrian circulation patterns substantially influences a host of mobile applications, including public navigational systems [1], Geospatial big data analytics [2], and social tracing in the era of epidemic [3]. Beside, the long-term navigation is also essential in the field of soldier positioning, which can ensure the safety of soldiers and improve the ability of person management under emergent scenarios.

Indoor positioning systems (IPSs) are capable of delivering consistent, real-time interior spatial data to the public. These systems are typically categorized into two types: those relying on wireless positioning mechanisms and those based on sensor-driven solutions. The former predominantly consists of technologies such as Wireless Fidelity (Wi-Fi) [4], Bluetooth Low Energy (BLE) [5], Ultra-wideband (UWB) [6], 5th generation mobile networks (5G) [7], inertial sensors [8], and acoustic sources [9]. These systems can offer diverse levels of precision in interior location data, though local infrastructure is often a prerequisite for the localization process. For instance, in the case of the fingerprinting method, the creation of a locally-focused wireless navigation database is vital. Similarly, knowledge about the positions of local wireless stations becomes crucial when employing time-measurement based techniques. Specifically, in highly challenging positioning scenarios where external wireless signals might be unavailable due to power scarcity, local wireless stations may fail to offer valuable location-centric information. This could result in the absence of uninterrupted indoor position data in such situations.

* Corresponding author.
E-mail address: michael-yue.yu@polyu.edu.hk (Y. Yu).
Peer review under responsibility of China Ordnance Society

https://doi.org/10.1016/j.dt.2024.05.006

Positioning systems driven by sensor technology are usually divided as magnetic matching (MM) [10], simultaneous localization and mapping (SLAM) [11], and dead-reckoning (DR) using inertial sensors [12]. MM based approach employs the characteristics of the surveyed magnetic map, aligned with specific geographic dispersion, and these generated magnetic characteristics will be synthesized into the magnetic fingerprint. However, the magnetic comparison method can be easily influenced by artificial indoor interference caused by alterations in urban conditions and human mobile devices. Additionally, the absence of radio identifiers would diminish the precision of real-world magnetic comparisons [13]. The SLAM technology typically comprises a camera module, an inertial measurement unit (IMU), and lidar modules, which are combined to gather environmental data under new circumstances. A drawback of the SLAM technology is that the efficiency of characteristics extraction in areas with indistinct features for instance corridors and tunnels. Additionally, alterations in lighting can disrupt the precision of data collection by the camera [14]. For DR systems based on inertial sensors, inexpensive commercial sensors are always amalgamated as the localization module, and are deployed at various places on the pedestrian. These systems can deliver high-precision location information over short periods without the need for any additional positioning stations, traits that have caught the interest of numerous scholars.

DR systems that rely on inertial sensors typically incorporate two predominant positioning methodologies: Pedestrian Dead Reckoning (PDR) [15] and the Inertial Navigation System (INS) infrastructure [16]. Traditional PDR infrastructure includes continuous fundamental stages: stride period identification, stride-length assessment, heading computing, and real-time position update. Unlike PDR, the INS infrastructure remains unaffected by variable handheld modes and doesn't necessitate stride-length parameters specific to individual users.

Renowned as two of the most widely accepted INS-based pedestrian navigation systems, the Waist-mounted Positioning System (WPS) and Foot-mounted Positioning System (FPS) are often employed in emergency rescue operations devoid of absolute positioning sources and facilities. One major issue is that the built-in sensors attached on the waist are normally cost-effective and the sensors biases tend to diverge over time. Furthermore, the prolonged positioning efficacy of current FPS and WPS is significantly hindered by accumulative sensor errors [17], disrupted local magnetic field [18], and intricate human motion patterns [19].

To conquer the challenges, various approaches are developed to enhance the performance of FPS and WPS. Yu et al. [20] compared the localization performance of FPS, WPS, and handheld built-in sensors, and several state-of-art filters are adopted for data fusion respectively. According to the comprehensive experiments, the waist-mounted approach realizes the higher accuracy than other two approaches, and different route path make an important influence for final trajectory. Kuang et al. [15] combines the PDR and INS mechanizations on the smartphone-based positioning platform, and extracted multiple observations for constraining the cumulative error of inertial and magnetic sensors, including external acceleration vector, QSMF, quasi-static status et al., which effectively improve the final positioning accuracy of low-cost sensors. Li et al. [21] developed an innovative integration structure combining sensors, Wi-Fi, and magnetic based positioning sources. A multi-tier quality-control (QC) criteria was employed to augment the efficacy and accuracy of the real-time positioning procedure, with the Root Mean Square Error (RMSE) of the developed structure averaging at 4.3 m across various environments.

Zero-velocity update (ZUPT) and zero angular rate update (ZARU) algorithms, core components of both FPS and WPS, are prevalent methods employed to mitigate the cumulative error prevalent in existing Strap-down Inertial Navigation Systems (SINS). Foxlin [22] first introduced the ZUPT to curb time-related positioning deviation of the FPS, the ZUPT constraint has since been extensively utilized in FPS for its superior performance. Typically, the ZUPT process encompasses two stages: quasi-static (QS) phase recognition and positioning error rectification. The Kalman filter (KF) is typically used to correct navigation errors utilizing the zero-velocity vector, achieving around 5% positioning accuracy compared to the overall distance with this approach. Consequently, efficient detection of QS periods has a more significant influence on the accuracy enhancement of ZUPT. A bimodal unscented Kalman filter was devised by Tong et al. [23] to mitigate attitude errors, while a hidden Markov algorithm was incorporated to improve the accuracy of the ZUPT, thereby ensuring a maximum positioning error not exceeding 2%. For enhancing the efficacy of gyroscope-based Attitude Determination and Control System (ADCS). Li et al. [24] introduced a self-calibration algorithm. The developed structure integrates a set of observational constraints, such as the pseudo observation, external acceleration, and ZUPT/ZARU, to significantly enhance the accuracy and stability of SINS.

In line with the ZUPT constraint, cumulative error of heading update cannot be eliminated, thereby failing to fully preserve the accuracy of inertial sensors. Consequently, researchers extract more observations for correcting heading deviation and estimating gyroscope bias. The ZARU constraint is presented to target the estimation of gyroscope bias [24]. However, ZARU performance depends on extended quasi-static (QS) periods typically not available in real-world scenarios. Unlike the unique modes in handheld mobile devices, Foot-Mounted Positioning Systems (FPSs) usually employ a steady deployment way. Therefore, the Non-Holonomic Constraint (NHC) constraint becomes applicable to enhance the performance of FPS. This algorithm is routinely utilized in vehicular and robotic navigation systems [25].

Beyond the scope of ZUPT/ZARU/NHC methodologies, magnetic observations are furnished by a built-in magnetometer for facilitating z-axis bias calibration for the gyroscope. The most quintessential filter in use would be the Complementary Filtering (CF) framework presented by Mahony [26], where calibrated magnetic data's observational vectors are designed to amend the heading divergence engendered by gyroscope-based estimates. However, this approach bears a significant downside, as magnetic field is substantially impacted by local artificial interference, leading to instability, thereby making it unsuitable for direct application in gyroscope bias estimation. Kuang et al. [18] presented a magnetometer bias-resistant magnetic field matching algorithm based on PDR for indoor smartphone localization. An INS-assisted PDR scheme is developed to estimate the locations and orientation of the smartphone. The relative trajectory information is employed to establish a correlation between the magnetic field sequences, enhancing their distinguishability. Additionally, the estimated orientation is applied to transform the reference magnetic field vector from the navigation frame (n-frame) to the body frame (b-frame). This enables the application of Magnetic Field Matching (MFM) in the b-frame, effectively mitigating the impact of magnetometer bias. Evaluations conducted on four smartphones through eight tests demonstrated that the proposed methodology successfully alleviated the bias-induced interference in MFM, resulting in an average positioning accuracy of 0.77 m (Root Mean Square (RMS)). Additionally, Yu et al. [27] enhanced CF's performance amidst areas featuring disturbed magnetic fields and complex human motion modes by adopting the Quality-based Sensor Measurements Fusion (QSMF) vector as the quality control factor, in tandem with the external acceleration vector. Experimental results indicated that the improved CF effectively boosted the accuracy of attitude estimations in complex environments and variable human

motion modes.

In contemporary times, urban structures usually offer interior blueprints for commercial use, and FPS based on indoor map-matching can to a certain extent, limit serious cumulative errors of direction and location, thereby enhancing the overall iLBSs experience. In such scenarios, the Particle Filter is considered a well-developed integration structure, which curtails the divergence in direction and position by regulating the update and dispersion of particles based on the constraint of map information [28]. Nonetheless, the map-matching method requires prior map data, and the precision of integrated results is influenced by the efficiency of useful information extraction of map, potentially leading to the introduction of additional observational errors.

The existing challenges of current researches are that the current algorithm cannot extract enough useful magnetic observations for heading calibration, and the low-precision walking speed estimation and multi-source fusion algorithm also cause the cumulative error under complex human motion. In an effort to surmount these aforementioned challenges, this paper introduces an innovative Data and Physical Model Dual-Driven Trajectory Estimation (DPDD-TE) framework. This system is capable of providing accurate positioning capabilities in indoor environments fraught with disturbances and consisting of multiple stories. The contributions of this study are summarized as follows:

1) A Bi-LSTM network is presented to improve the efficacy of local magnetic field interference detection. By processing related features derived from built-in sensors and magnetometers which serve as input vectors for Bi-LSTM for training and predictive purposes, the recognized Quasi-Static Magnetic Field (QSMF) periods are further modelled as magnetic observations to calibrate heading directions.
2) This paper proposes Bi-LSTM network based walking speed prediction model, which considers all the raw data and extracted human motion features provided by waist-mounted inertial sensors and can provide much more accurate walking speed information than the traditional approaches.
3) This article introduces multi-tier observables, such as QSMF, gait-length, and position change, as well as multi-tier constraints which include ZUPT/ZARU, altitude restriction, and NHC. These observations and constraint are combined with the INS infrastructure to mitigate the impacts of divergence and cumulative errors, magnetic interference, and external accelerations originating from the inertial sensors.
4) Leveraging the estimation outcome of QSMF detection, walking speed appraisal, and hybrid observations, the DPDD-TE methodology is developed. A unified Unscented Kalman Filter (UKF) is utilized to consolidate the INS infrastructure alongside the above observables and constraints, which is further enhanced by a loop detection algorithm assisted by magnetic and trajectory features. The amalgamation of multiple models effectively augments the accuracy and stability of the presented DPDD-TE.

The overall algorithm structure of proposed DPDD-TE is described in Fig. 1.

This work is organized as follows: Section 2 expounds upon the development of the Bi-LSTM-based QSMF detection and velocity estimation. Section 3 proposes an indoor localization framework built upon a mix of observations and restrictions. Section 4 introduces an infrastructure for localization and optimization that is guided by both data and physical models. In Section 5, the experimental results of the presented DPDD-TE are detailed. Finally, Section 6 provides a conclusion to the paper and outlines directions for future research.

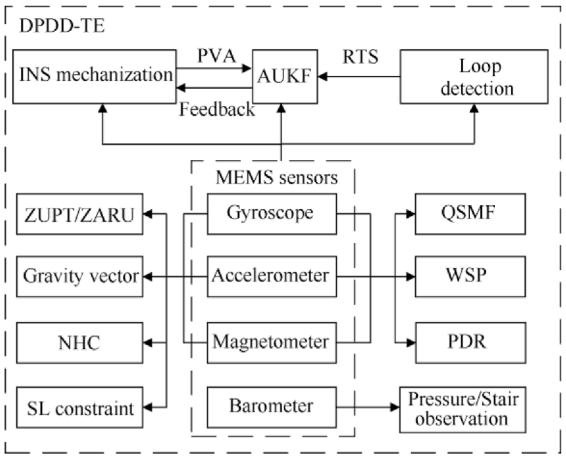

Fig. 1. Overall algorithm procedure of proposed DPDD-TE.

2. Bi-LSTM based QSMF recognition and walking speed prediction algorithm

In this part, we present a robust Bi-LSTM approach for recognition of QSMF phase among the time periods of the human's walking mode, and can also predict the walking speed of the pedestrian using raw sensors data and extracted human motion features.

2.1. Bi-LSTM based QSMF recognition

The detection of QSMF is a crucial step in heading calibration, as it greatly impacts the accuracy of final positioning and attitude estimation. In this study, we present a Bi-LSTM architecture for precise detection of quasi-static periods, utilizing the wealth of features available from inertial sensors. The detailed description of the Bi-LSTM structure can be found in Ref. [29]:

Fig. 2 describes the primary architecture of the proposed QSMF period detection approach using Bi-LSTM network. In this approach, the input features are formed from the motion information of built-in sensors, while the output value of the Bi-LSTM represents the QSMF recognition results of the captured trajectories. The specific details of the input and output vectors are described as follows

1) Acceleration vector acquired from built-in accelerometer along the x-axis, y-axis, and z-axis, a_x, a_y and a_z.
2) Rotation rate vector acquired from built-in gyroscope along the x-axis, y-axis, and z-axis g_x, g_y, g_z.
3) Magnetic vector acquired from built-in magnetometer along the x-axis, y-axis, and z-axis m_x, m_y, m_z.
4) Norm of collected accelerometer data

$$Norm_{\text{acc}} = \sqrt{a_x{}^2 + a_y{}^2 + a_z{}^2} \tag{1}$$

5) Norm of collected gyroscope data

$$Norm_{\text{gyro}} = \sqrt{g_x{}^2 + g_y{}^2 + g_z{}^2} \tag{2}$$

6) Norm of collected magnetometer data

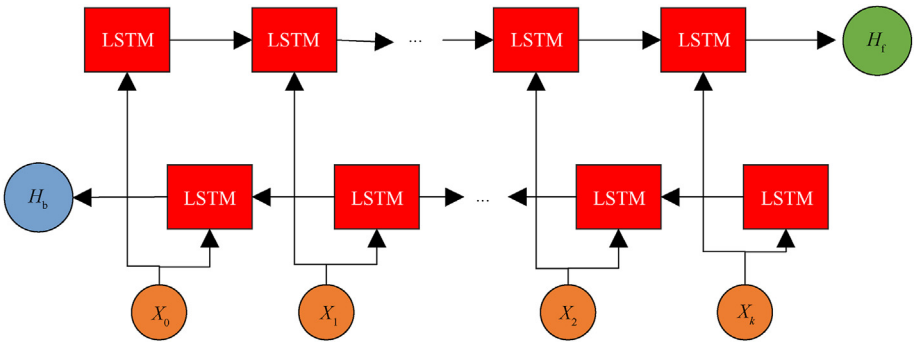

Fig. 2. Structure of Bi-LSTM network.

$$Norm_{\mathrm{mag}} = \sqrt{m_x{}^2 + m_y{}^2 + m_z{}^2} \tag{3}$$

7) Variance of acceleration norm

$$(S_{\mathrm{acc}})^2 = \frac{\sum_{i=1}^{n}\left[(Norm_{\mathrm{acc}}(i) - \overline{Norm_{\mathrm{acc}}(i)})^2\right]}{(n-1)} \tag{4}$$

8) Variance of rotation rate norm:

$$(S_{\mathrm{gyro}})^2 = \frac{\sum_{i=1}^{n}\left[(Norm_{\mathrm{gyro}}(i) - \overline{Norm_{\mathrm{gyro}}(i)})^2\right]}{(n-1)} \tag{5}$$

9) Variance of magnetometer norm

$$(S_{\mathrm{mag}})^2 = \frac{\sum_{i=1}^{n}\left[(Norm_{\mathrm{mag}}(i) - \overline{Norm_{\mathrm{mag}}(i)})^2\right]}{(n-1)} \tag{6}$$

10) Interquartile range (IQR) of acceleration norm

$$IQR_{\mathrm{acc}} = Q_3^{\mathrm{acc}} - Q_1^{\mathrm{acc}} \tag{7}$$

11) IQR of rotation rate norm

$$IQR_{\mathrm{gyro}} = Q_3^{\mathrm{gyro}} - Q_1^{\mathrm{gyro}} \tag{8}$$

12) IQR of magnetometer norm

$$IQR_{\mathrm{mag}} = Q_3^{\mathrm{mag}} - Q_1^{\mathrm{mag}} \tag{9}$$

The described features are built based on the sensors data from accelerometer, gyroscope, and magnetometer, which are further applied for Bi-LSTM model training and prediction, and the specific parameters of presented Bi-LSTM network are described as follows [29].

$$\begin{cases} f_t = \sigma\cdot\left(W_f\cdot h_{t-1} + U_f\cdot X_t + b_f\right) \\ i_t = \sigma\cdot(W_i\cdot h_{t-1} + U_i\cdot X_t + b_i) \\ a_t = \tanh\,(W_a\cdot h_{t-1} + U_a\cdot X_t + b_a) \\ \tilde{C}_t = \tilde{C}_{t-1}\cdot f_t + i_t\cdot a_t \\ o_t = \sigma\cdot(W_o\cdot h_{t-1} + U_o\cdot X_t + b_o) \\ h_t = o_t\cdot\tanh(C_t) \\ \hat{y}_t = \sigma(Vh_t + c) \end{cases} \tag{10}$$

where i_t, f_t, o_t are the input, forget and output gate parameters, X_t is the built input vector of Bi-LSTM model at the timestamp t, and the h_t indicates the hidden state vector. σ is the sigmoid function, and C_t is the memorized state, which is combined with output vector as the memorized state at timestamp t.

The output layer of the proposed Bi-LSTM units is modelled as the input vector of the fully-connected network

$$\widehat{H}_i = fully - connected(y_i) \tag{11}$$

Finally, as the output vector of QSMF detection algorithm, the QSMF index $\widehat{H}_i$ is presented as the final predicted result of QSMF detection as 1 or 0.

2.2. Bi-LSTM assisted walking speed predictor

In this paper, the Bi-LSTM based walking speed predictor (WSP) is developed for the walking speed prediction based on the consideration of complex human motion, the final predicted walking speed information is defined as

$$v_t = full - connected(y_t) \tag{12}$$

In which v_t represents the predicted walking velocity. To get better performance of speed estimation, following features are extracted to adaptively describe the motion characteristics of the pedestrian wearing waist-mounted inertial sensors.

Prior to feeding the inertial sensor data with the Bi-LSTM structure, a preprocessing step is required to reduce complexity of input vector, allowing for a better fit to the human walking mode. The proposed walking speed estimator utilizes the 9-axis motion data to transform from the b-frame to the n-frame using the attitude quaternion. Eq. (13) can be employed to convert the vector AG_{INS} from the b-frame to the corresponding variable in the n-frame:

$$AG_{\mathrm{INS}} = \boldsymbol{q} \times AG_{\mathrm{IMU}} \times \boldsymbol{q}^{-} \tag{13}$$

in Eq. (13), the transformed IMU data is referred to as AG_{INS} and serves as the input values for the presented walking speed estimator.

To enhance the update frequency of velocity estimation, this study adopts the sliding window technique. By employing a constant time period (1 s) of sensor data with sampling rate of 100 Hz, which is segmented into independent sequences. This approach increases the output frequency to 20 Hz. To ensure stability, the output is subsequently subjected to low-pass filter.

In addition, the walking velocity vector predicted by the waist-mounted node by the linear and non-linear models

$$\begin{cases} S_1 = \dfrac{\alpha \cdot \left[0.7 + \beta(H - 1.75) + \varsigma \cdot \dfrac{(F_t - 1.79)H}{1.75}\right]}{t_1 - t_0} \\ S_2 = \dfrac{K\sqrt[4]{A_{\max} - A_{\min}}}{t_1 - t_0} \end{cases} \tag{14}$$

In which the α, β, ς indicate the human feature-related parameters, F_t indicates the step frequency, and H indicates the user's height value. $A_{\max}$ and $A_{\min}$ represent the recognized peak and valley vectors acquired from acceleration under the detected step period, K indicates the scale parameters for different users. Besides, Norm of collected accelerometer data provided by the waist-mounted module is also selected as one of the input features:

$$Norm_{\mathrm{acc}} = \sqrt{a_x^2 + a_y^2 + a_z^2} \tag{15}$$

where $Norm_{\mathrm{acc}}$ indicates the calculated norm of the acceleration vector, and is also modelled as the one of the input values of developed walking speed estimator.

3. MEMS sensors-based multi-level observations and constraints

In this section, we extract and model hybrid observations and constraints as robust constraints in the proposed DPDD-TE multi-source fusion model. This approach aims to decrease the cumulative error originated from sensor errors, as well as the complex motion of humans and indoor environments.

3.1. Hybrid constraints for proposed DPDD-TE

The real-world magnetic field is usually disturbed in most complex environments because of the artificial interference, while the detected QSMF time periods among the pedestrian's walking procedure can provide short-term precise local magnetic field reference for sensors bias calibration [24]. In this case, the first timestamp of recognized QSMF phase is modelled as the absolute observation vector

$$\boldsymbol{M}^n_{\mathrm{refer}} = \boldsymbol{\psi}^n_{b,1} \cdot \boldsymbol{M}^b_{k,1} \tag{16}$$

where $\boldsymbol{M}^b_{k,1}$ is the magnetic data extracted from the initial phase of the QSMF period and represent the attitude matrix $\boldsymbol{\psi}^n_{b,1}$ calculated at the following phases. Thus, the observation model can be built according to the following QSMF phases

$$\delta \boldsymbol{Z}^n_M = \boldsymbol{\psi}^n_{b,k} \cdot \boldsymbol{M}^b_k - \boldsymbol{M}^n_{\mathrm{refer}} = (\mathbf{I} - \boldsymbol{\theta} \times)\boldsymbol{\psi}^n_{b,k}\left(\boldsymbol{m}^b_k + \boldsymbol{\varepsilon}_m\right) - \boldsymbol{m}^n_{\mathrm{refer}} = \Big[\times \left(\boldsymbol{\psi}^n_{b,k}\boldsymbol{M}^b_k\right) \times \Big]\boldsymbol{\theta} + \boldsymbol{\psi}^n_{b,k}\boldsymbol{\varepsilon}_m \tag{17}$$

where $\boldsymbol{M}^b_k$ denote the magnetic data collected during the identified QSMF period, $\boldsymbol{\psi}^n_{b,1}$ represent the estimated attitude matrix at the current timestamp, $\boldsymbol{\varepsilon}_m$ and $\Delta \boldsymbol{D}_m = norm(\boldsymbol{M}^b_k - \boldsymbol{M}^n_{\mathrm{refer}})$ represent the adaptive adjustment of measurement noise for the collected magnetic data based on the disparity among the acquired magnetic vector and the reference real-world magnetic field.

The external acceleration exists under human's motion procedure using DPDD-TE, which would lead to the cumulative error of roll and pitch angles calculation and update. In this case, the external acceleration is adopted and modelled as the observation combined with the local gravity vector [15].

$$\delta \boldsymbol{f}^n = \boldsymbol{f}^n - \widehat{\boldsymbol{\psi}}^n_b \tilde{\boldsymbol{f}}^b \approx \boldsymbol{f}^n - (\mathbf{I} - [\boldsymbol{\theta} \times])\boldsymbol{\psi}^n_b \boldsymbol{f}^b + \boldsymbol{\psi}^n_b \boldsymbol{\varepsilon}_a = [\boldsymbol{\theta} \times]\boldsymbol{f}^n + \boldsymbol{\psi}^n_b \boldsymbol{\varepsilon}_a = [\boldsymbol{f}^n \times]\boldsymbol{\theta} + \boldsymbol{\psi}^n_b \boldsymbol{\varepsilon}_a \tag{18}$$

where $\boldsymbol{f}^n$ presents the reference gravity vector, $\tilde{\boldsymbol{f}}^b$ is the outputted acceleration vector, $\boldsymbol{\theta}$ indicates the attitude angle vector, $\boldsymbol{\psi}^n_b$ indicates the attitude matrix, and the noise of acceleration $\boldsymbol{\varepsilon}_a$ is modelled according to the extraction of external acceleration

$$\boldsymbol{\varepsilon}_a = \begin{cases} \kappa_a & N_a \le \lambda_{01} \\ \left({N_a}^2 / P\right)\kappa_a & \lambda_{01} < N_a \le \lambda_{02} \\ \infty & N_a > \lambda_{02} \end{cases} \tag{19}$$

where $N_a = \left| norm(\boldsymbol{f}^b) - \boldsymbol{g} \right|$ is the modelled observation of external acceleration, κ_a is the bias stability of the accelerometer, P is the error covariance acquired from AUKF.

In this study, a 1D Convolutional Neural Network (1D-CNN) is utilized for the recognition of the QS phase during the walking procedure of pedestrians [12]. Once the QS phases are recognized and labeled, ZUPT constraint is constructed as

$$\delta \boldsymbol{Z}^n_v = \boldsymbol{v}^n_{\mathrm{INS}} - [0 \quad 0 \quad 0]^{\mathrm{T}} = \delta \boldsymbol{v}^n + n_v \tag{20}$$

where $\boldsymbol{v}^n_{INS}$ indicate the raw INS estimated 3D velocity.

To effectively decrease the bias divergence of gyroscope under QS phases, the ZARU constraint is also constructed [24].

$$\delta \boldsymbol{Z}_\vartheta = \vartheta^n_{\mathrm{INS}} - \vartheta^n_{\mathrm{refer}} = \delta\vartheta + n_\vartheta \tag{21}$$

where $\vartheta^n_{\mathrm{INS}}$ is the INS provided heading value, $\vartheta^n_{\mathrm{refer}}$ is the first heading value of QS phase, and n_ϑ is the measurement noise.

NHC is normally applied to enhance the solvency ability of INS under various navigation fields according to the principle that the measurement speed when moving forward is generally zero [26]. In this work, the estimated velocity vector in b-frame is described as

$$\boldsymbol{\nu}^b = \left[\nu^b_{\mathrm{forward}} \quad 0 \quad 0\right]^{\mathrm{T}} \tag{22}$$

where ν^b_{forward} indicates the original estimated velocity under b-frame. Then the original estimated velocity under b-frame is converted to n-frame using current attitude matrix

$$\boldsymbol{v}^n = \boldsymbol{\varpi}_b^n \boldsymbol{v}^b \tag{23}$$

where $\boldsymbol{\varpi}_b^n$ indicates the calculated attitude matrix from b-frame to n-frame, $\boldsymbol{v}^n$ is final converted velocity vector.

To enhance the positioning performance, the straight-line constraint is extracted to limit the cumulative error under the regular walking route. Moreover, in this research, heading information calculated from adjacent gait periods is recorded for straight-line recognition

$$\boldsymbol{L}_1 = \begin{cases} 1 & \max\{|\boldsymbol{\theta}^s - \text{mean}(\boldsymbol{\theta}^s)|\} < T_{1,\theta} \\ 0 & \text{others} \end{cases} \tag{24}$$

$$\begin{cases} \boldsymbol{\theta}^s = \{\boldsymbol{\theta}_{m-4}^s, \boldsymbol{\theta}_{m-3}^s, \cdots, \boldsymbol{\theta}_m^s\} \\ \boldsymbol{\theta}_m^s = a\tan 2\left(\boldsymbol{r}_{y,m}^n - \boldsymbol{r}_{y,m-1}^n, \boldsymbol{r}_{x,m}^n - \boldsymbol{r}_{x,m-1}^n\right) \end{cases} \tag{25}$$

where $(\boldsymbol{r}_{x,m}^n, \boldsymbol{r}_{y,m}^n)$ represents the mth step position calculated by WPS, if $\boldsymbol{L}_1 = 1$, the user is recognized as walking alongside a straight network.

3.2. Hybrid observations for proposed DPDD-TE

Due to the rapid divergence error observed in conventional INS mechanization, the estimated velocity exhibits fast divergence over time. Consequently, we adopt the PDR originated step-length for generating the speed observation [27].

$$\boldsymbol{V}_{\text{PDR}} = \begin{bmatrix} \dfrac{\alpha_s}{\mu_1 - \mu_0} & 0 & 0 \end{bmatrix} \tag{26}$$

In Eq. (26), $\boldsymbol{V}_{\text{PDR}}$ indicates the computed walking speed obtained through PDR mechanization. μ_1 and μ_0 denote the timestamps extracted from start and last phases.

In addition, the PDR originated location update results are also modelled as the observation equation

$$\begin{bmatrix} \boldsymbol{r}_x(k) \\ \boldsymbol{r}_y(k) \end{bmatrix} = \begin{bmatrix} \boldsymbol{r}_x(k-1) \\ \boldsymbol{r}_y(k-1) \end{bmatrix} + \alpha_s(t) \begin{bmatrix} \cos(\vartheta(k)) \\ \sin(\vartheta(k)) \end{bmatrix} \tag{27}$$

In Eq. (27), the location observation provided by the PDR system is denoted as $(\boldsymbol{r}_x(k), \boldsymbol{r}_y(k))$, represent the observed coordinates in the x and y directions, respectively. Furthermore, $\alpha_s(t)$ represents the linear gait-length value estimated by the PDR system, while $\vartheta(k)$ denotes the heading information.

The observation model is formulated based on the PDR-provided speed and location information as follows

$$\begin{cases} \delta \boldsymbol{Z}_v^n = \boldsymbol{v}_{\text{PDR}}^n - \boldsymbol{v}_{\text{INS}}^n \\ \delta \boldsymbol{Z}_p^n = \boldsymbol{p}_{\text{PDR}}^n - \boldsymbol{p}_{\text{INS}}^n \end{cases} \tag{28}$$

where $\boldsymbol{v}_{\text{PDR}}^n$ and $\boldsymbol{p}_{\text{PDR}}^n$ represent the PDR related walking velocity and position increment; $\boldsymbol{v}_{\text{INS}}^n$ and $\boldsymbol{p}_{\text{INS}}^n$ indicate the INS estimated speed and location information.

In the presented DPDD-TE algorithm, the estimated walking speed by Bi-LSTM is adopted as the observation model

$$\begin{cases} \delta \boldsymbol{Z}_v^n = \boldsymbol{v}_{\text{LSTM}}^n - \boldsymbol{v}_{\text{INS}}^n \\ \delta \boldsymbol{Z}_p^n = \boldsymbol{p}_{\text{LSTM}}^n - \boldsymbol{p}_{\text{INS}}^n \end{cases} \tag{29}$$

where $\boldsymbol{v}_{\text{LSTM}}^n$ and $\boldsymbol{p}_{\text{LSTM}}^n$ are the Bi-LSTM originated velocity and related position vectors, $\boldsymbol{v}_{\text{INS}}^n$ and $\boldsymbol{p}_{\text{INS}}^n$ velocity and related position vectors originated from INS algorithm.

When the pedestrian moves under 3D environments, for the waist-mounted positioning system, the barometer provided altitude constraint is also extracted for error control [27].

$$\delta \boldsymbol{z}_h^n = h_B^n - h_{\text{INS}}^n \tag{30}$$

where h_B^n indicates the barometer-originated altitude calculation, h_{INS}^n indicates the z-axis location change estimated by WPS.

4. Positioning structure of DPDD-TE

In this section, we present the loop detection algorithm that incorporates a corner detection method for trajectory optimization. Furthermore, we introduce a dual-driven structure based on data and physical models to facilitate efficient multi-source fusion. The proposed DPDD-TE framework consists of multiple phases, including multi-source fusion and optimization, to deliver precise waist-mounted 3D indoor localization performance.

4.1. Loop detection algorithm

To ensure the absolute location of the pedestrian with waist-mounted equipment, the corner detection algorithm is firstly applied for initial location detection and trajectory calibration. The combination of Dynamic Time Warping (DTW) and Pearson correlation coefficient (PCC) is regarded as an effective approach for trajectory matching according to similarity analysis [30]. In our study, the map matching algorithm comprises two key components: corner recognition and pedestrian network matching. To enhance the detection accuracy, we combine the DTW and PCC indices to realize corner recognition, which is outlined as follows:

Corner matching using DTW: The movement trajectories are represented as sequences with extracted motion and acquired magnetic features:

$$\boldsymbol{S}_{\text{temp}} = \begin{bmatrix} x_1 & x_{k-m+1} & \cdots & x_k & x_{k+1} & \cdots & x_{k+m} \\ y_1 & y_{k-m+1} & \cdots & y_k & y_{k+1} & \cdots & y_{k+m} \\ m_1 & m_{k-m+1} & \cdots & m_k & m_{k+1} & \cdots & m_{k+m} \end{bmatrix} \tag{31}$$

The reference sequence is built according to the prior information

$$\boldsymbol{S}_{\text{test}} = \begin{bmatrix} \chi_1 & \chi_{k-m+1} & \cdots & \chi_k & \chi_{k+1} & \cdots & \chi_{k+m} \\ \gamma_1 & \gamma_{k-m+1} & \cdots & \gamma_k & \gamma_{k+1} & \cdots & \gamma_{k+m} \\ \eta_1 & \eta_{k-m+1} & \cdots & \eta_k & \eta_{k+1} & \cdots & \eta_{k+m} \end{bmatrix} \tag{32}$$

The DTW index is calculated based on $\boldsymbol{S}_{\text{temp}}$ and $\boldsymbol{S}_{\text{test}}$.

$$d_{ij} = (\chi_i - x_j)^2 + \left(\gamma_i - y_j\right)^2 + (\eta_i - m_j)^2 \tag{33}$$

In which d_{ij} indicates ith row and jth column value.

Corner matching based on PCC: The suitability of trajectories derived from DTW is subsequently assessed using PCC, which characterizes the similarity between the two matched sequences as follows

$$corrcoef\left(V_{\text{temp}}, V_{\text{test}}\right) = \frac{\sum_{i=1}^{M}\left(V_{\text{temp}}^{i} - \overline{V}_{\text{temp}}\right)\left(V_{\text{test}}^{i} - \overline{V}_{\text{test}}\right)}{\sqrt{\sum_{i=1}^{M}\left(V_{\text{temp}}^{i} - \overline{V}_{\text{temp}}\right)^{2}}\sqrt{\sum_{i=1}^{2m+1}\left(V_{\text{test}}^{i} - \overline{V}_{\text{test}}\right)^{2}}} \tag{34}$$

where i indicates i^{th} value of V_{temp} or V_{test}. The correlation results are calculated separately. Once a loop point has been detected, the RTS based trajectory optimization algorithm is applied for trajectory smoothing for error elimination.

4.2. Overall structure of DPDD-TE

In this work, for the overall structure of DPDD-TE, the INS mechanization is adopted as the main model for 3D position and attitude update, which is described as follows [15].

$$\begin{bmatrix} \dot{\xi}^{n} \\ \dot{v}^{n} \\ \dot{\psi}_{b}^{n} \end{bmatrix} = \begin{bmatrix} \boldsymbol{\varpi}^{-1}\boldsymbol{v}^{n} \\ \boldsymbol{\psi}_{b}^{n}\boldsymbol{f}^{b} - (2\boldsymbol{\omega}_{ie}^{n} + \boldsymbol{\omega}_{en}^{n})\boldsymbol{v}^{n} + \boldsymbol{g}^{n} \\ \boldsymbol{\psi}_{b}^{n}\left(\boldsymbol{\omega}_{ib}^{b} - \boldsymbol{\omega}_{in}^{b}\right) \end{bmatrix} \tag{35}$$

where $\boldsymbol{\xi}^{n} = [\,\xi_{N} \quad \xi_{E} \quad \xi_{D}\,]^{\mathrm{T}}$ represents the 3D location of the users in n-frame; $\boldsymbol{v}^{n} = [\,v_{N} \quad v_{E} \quad v_{D}\,]^{\mathrm{T}}$ is the updated 3D velocity of the users in n-frame; and $\boldsymbol{\psi}_{b}^{n}$ is the updated attitude information; $\boldsymbol{g}^{n}$ is the reference gravity value.

The Earth-related definitions $\boldsymbol{\omega}_{ie}^{n}$ and $\boldsymbol{\omega}_{en}^{n}$ can be omitted due to the large noise of MEMS sensors, therefore the state update model of presented DPDD-TE is described as [1]

$$\begin{cases} \delta\dot{\boldsymbol{\xi}}^{n} = -\boldsymbol{\omega}_{en}^{n} \times \delta\boldsymbol{\xi}^{n} + \delta\boldsymbol{v}^{n} \\ \delta\dot{\boldsymbol{v}}^{n} = -(2\boldsymbol{\omega}_{ie}^{n} + \boldsymbol{\omega}_{en}^{n})\delta\boldsymbol{v}^{n} + \boldsymbol{f}^{n} \times \boldsymbol{\theta} + \boldsymbol{C}_{b}^{n}(\boldsymbol{\varepsilon}_{a} + \boldsymbol{\varpi}_{ba}) \\ \dot{\boldsymbol{\theta}} = -(\boldsymbol{\omega}_{ie}^{n} + \boldsymbol{\omega}_{en}^{n}) \times \boldsymbol{\theta} - \boldsymbol{\psi}_{b}^{n}\left(\boldsymbol{\alpha}_{g} + \boldsymbol{\varpi}_{bg}\right) \\ \dot{\boldsymbol{\alpha}}_{g} = \boldsymbol{\alpha}_{g} \big/ \tau_{bg} + \boldsymbol{\varpi}_{bg} \\ \dot{\boldsymbol{\alpha}}_{a} = -\boldsymbol{\alpha}_{a}/\tau_{ba} + \boldsymbol{\varpi}_{ba} \end{cases} \tag{36}$$

where $\delta\boldsymbol{\xi}^{n}$, δv^{n}, and θ are the modelled state errors of 3D location, velocity, and attitude; α_{g} and α_{a} indicate the sensors biases; $\boldsymbol{f}^{n}$ indicates the converted the acceleration vector, ϖ_{bg} and ϖ_{ba} are the related Gaussian noise. The state vector of DPDD-TE is modelled as

$$\delta\boldsymbol{X} = \left[\ (\delta\boldsymbol{\xi}^{n})_{1\times3} \quad (\delta v^{n})_{1\times3} \quad \boldsymbol{\theta}_{1\times3} \quad (\boldsymbol{\alpha}_{g})_{1\times3} \quad (\boldsymbol{\alpha}_{a})_{1\times3}\ \right]^{\mathrm{T}} \tag{37}$$

The discrete-time state equation and observation equation are described as follows

$$\begin{cases} \delta\boldsymbol{X}_{k} = \boldsymbol{F}_{k-1,k}\delta\boldsymbol{X}_{k-1} + \gamma_{k} \\ \delta\boldsymbol{Z}_{k} = \boldsymbol{G}_{k}\delta\boldsymbol{X}_{k} + \iota_{k} \end{cases} \tag{38}$$

where $\delta\boldsymbol{X}_{k}$ and $\delta\boldsymbol{Z}_{k}$ indicate the state vector and observation vector; $\boldsymbol{G}_{k}$ and $\boldsymbol{F}_{k-1,k}$ indicate the observation matrix and state transition matrix

$$\boldsymbol{F}_{k-1,k} = \begin{bmatrix} \mathbf{I}_{3\times3} & \mathbf{I}_{3\times3}\times\Delta t & 0_{3\times3} & 0_{3\times3} & 0_{3\times3} \\ 0_{3\times3} & \mathbf{I}_{3\times3} & (\boldsymbol{f}_{k}^{n}\times)\cdot\Delta t & 0_{3\times3} & 0_{3\times3} \\ 0_{3\times3} & 0_{3\times3} & \mathbf{I}_{3\times3} & -\boldsymbol{C}_{b,k}^{n}\cdot\Delta t & 0_{3\times3} \\ 0_{3\times3} & 0_{3\times3} & 0_{3\times3} & \mathbf{I}_{3\times3} & 0_{3\times3} \\ 0_{3\times3} & 0_{3\times3} & 0_{3\times3} & 0_{3\times3} & \mathbf{I}_{3\times3} \end{bmatrix} \tag{39}$$

where Δt indicates the sampling rate of presented DPDD-TE; $\boldsymbol{f}_{k}^{n}$ indicates converted the acceleration vector.

Finally, the updated state vector is applied for error feedback to the INS provided 3D location, velocity, and attitude

$$P_{b_{u+1}}^{b_{u}} \approx \widehat{P}_{b_{u+1}}^{b_{u}} + \boldsymbol{J}_{b_{a}}^{P}\delta b_{a_{u}} + \boldsymbol{J}_{b_{w}}^{P}\delta b_{w_{u}} \tag{40}$$

$$V_{b_{u+1}}^{b_{u}} \approx \widehat{V}_{b_{u+1}}^{b_{u}} + \boldsymbol{J}_{b_{a}}^{V}\delta b_{a_{u}} + \boldsymbol{J}_{b_{w}}^{V}\delta b_{w_{u}} \tag{41}$$

$$\varphi_{b_{u+1}}^{b_{u}} \approx \widehat{\varphi}_{b_{u+1}}^{b_{u}} \otimes \begin{bmatrix} 1 \\ \frac{1}{2}\boldsymbol{J}_{b_{w}}^{\varphi}\delta b_{w_{u}} \end{bmatrix} \tag{42}$$

According to Eqs. (40)–(42), the sensor bias errors are effectively decreased, and the original performance 3D location, velocity, and attitude can be significantly improved.

4.3. Data fusion and optimization model of DPDD-TE

In the presented DPDD-TE system, the INS is applied as the state equation to estimate the baseline 3D pose of the pedestrian. However, the raw measurements are susceptible to cumulative sensor errors, magnetic data disturbances, and external accelerations. To mitigate these errors, we propose multi-level observations and constraints to generate the hybrid observation equation. Furthermore, we employ AUKF to combine the state and observation models, enabling the DPDD-TE system to provide accurate location and attitude estimates.

To further enhance the accuracy of the DPDD-TE system provided forward trajectory estimation, we employ Recursive Trajectory Smoothing (RTS) when a loop route is detected. The entire AUKF-based forward trajectory calculation and RTS smoothing processes are presented as follows.

1) Parameters Initialization

$$\begin{cases} \widehat{\boldsymbol{x}}_{0} = E[\boldsymbol{x}_{0}] \\ \boldsymbol{P}_{0} = E\left[(\boldsymbol{x}_{0} - \widehat{\boldsymbol{x}}_{0})(\boldsymbol{x}_{0} - \widehat{\boldsymbol{x}}_{0})^{\mathrm{T}}\right] \end{cases} \tag{43}$$

2) Sigma Points Calculation

$$\boldsymbol{X}_{k-1}=\left(\widehat{\boldsymbol{x}}_{k-1},\widehat{\boldsymbol{x}}_{k-1}+\gamma\sqrt{\boldsymbol{P}_{k-1}},\widehat{\boldsymbol{x}}_{k-1}-\gamma\sqrt{\boldsymbol{P}_{k-1}}\right) \tag{44}$$

where $\boldsymbol{P}_{k\text{-}1}$ is the covariance matrix of AUKF, γ is the related scale factor.

3) State Model Update

$$\boldsymbol{X}_{k|k-1}^{i}=\boldsymbol{\varphi}\boldsymbol{X}_{k-1}^{i} \tag{45}$$

$$\boldsymbol{x}_{k}^{-}=\sum_{i=0}^{2n+1}\omega_i\boldsymbol{X}_{k|k-1}^{i} \tag{46}$$

$$\boldsymbol{P}_{k}^{-}=\sum_{i=0}^{2n+1}\omega_i\left(\boldsymbol{X}_{k|k-1}^{i}-\widehat{\boldsymbol{x}}_{k}^{-}\right)\left(\boldsymbol{X}_{k|k-1}^{i}-\widehat{\boldsymbol{x}}_{k}^{-}\right)+\boldsymbol{G}\boldsymbol{Q}_{k}\boldsymbol{G}^{\mathrm{T}} \tag{47}$$

$$\boldsymbol{Z}_{k|k-1}^{i}=h\left(\boldsymbol{X}_{k|k-1}^{i}\right) \tag{48}$$

$$\boldsymbol{z}_{k}^{-}=\sum_{i=0}^{2n+1}\omega_i\boldsymbol{Z}_{k|k-1}^{i} \tag{49}$$

4) Measurement Update:

$$\boldsymbol{P}_{\tilde{z}_k\tilde{z}_k}=\sum_{i=0}^{2n+1}\omega_i\left(\boldsymbol{Z}_{k|k-1}^{i}-\widehat{\boldsymbol{z}}_{k}^{-}\right)\left(\boldsymbol{Z}_{k|k-1}^{i}-\widehat{\boldsymbol{z}}_{k}^{-}\right)+\boldsymbol{R}_{k} \tag{50}$$

$$\boldsymbol{P}_{x_kz_k}=\sum_{i=0}^{2n+1}\omega_i\left(\boldsymbol{X}_{k|k-1}^{i}-\widehat{\boldsymbol{x}}_{k}^{-}\right)\left(\boldsymbol{Z}_{k|k-1}^{i}-\widehat{\boldsymbol{z}}_{k}^{-}\right)^{\mathrm{T}} \tag{51}$$

$$\boldsymbol{K}_{k}=\boldsymbol{P}_{x_kz_k}\boldsymbol{P}_{\tilde{z}_k\tilde{z}_k}^{-1} \tag{52}$$

$$\widehat{\boldsymbol{x}}_{k}=\widehat{\boldsymbol{x}}_{k}^{-}+\boldsymbol{K}_{k}(\boldsymbol{z}_{k}-\widehat{\boldsymbol{z}}_{k}^{-}) \tag{53}$$

$$\boldsymbol{P}_{k}=\boldsymbol{P}_{k}^{-}-\boldsymbol{K}_{k}\boldsymbol{P}_{\tilde{z}_k\tilde{z}_k}(\boldsymbol{K}_{k})^{\mathrm{T}} \tag{54}$$

5) RTS Based Trajectory Smoothing

$$\widehat{\boldsymbol{x}}_{k-1|k}=\widehat{\boldsymbol{x}}_{k-1}+\boldsymbol{P}_{k-1}(\boldsymbol{\varphi}_{k})^{\mathrm{T}}\left(\boldsymbol{P}_{k-1}^{-}\right)^{-1}\left(\widehat{\boldsymbol{x}}_{k}-\widehat{\boldsymbol{x}}_{k}^{-}\right) \tag{55}$$

$$\begin{aligned}\boldsymbol{P}_{k-1|k}=&\boldsymbol{P}_{k-1}-\left(\boldsymbol{P}_{k-1}(\boldsymbol{\varphi}_{k})^{\mathrm{T}}(\boldsymbol{P}_{k}^{-})^{-1}\right)\\&\times(\boldsymbol{P}_{k}-\boldsymbol{P}_{k}^{-})\cdot\left(\boldsymbol{P}_{k-1}(\boldsymbol{\varphi}_{k})^{\mathrm{T}}(\boldsymbol{P}_{k}^{-})^{-1}\right)^{\mathrm{T}}\end{aligned} \tag{56}$$

where $\boldsymbol{x}_k$ and $\boldsymbol{z}_k$ indicate the state vector and measured vector. Eqs. (43)–(54) describe the forward trajectory estimation, and Eqs. (55) and (56) describe the RTS based trajectory smoothing using loop recognition results.

5. Experiment results of DPDD-TE

In order to assess the accuracy and effectiveness of the presented DPDD-TE method, a series of experiments are devised to compare it with state-of-the-art approaches. The experiments are conducted in a multi-floor building, chosen for its comprehensive nature, and conducted over a long-term period across different floors. To introduce a controlled interference, an artificial magnetic field disturbance is applied during the experiments. Fig. 3 illustrates the hardware employed in our waist-mounted system, while Table 1 presents the key technical specifications of the inertial sensors utilized.

Fig. 3. Marked QS periods of selected trajectory.

Table 1
Hardware features of waist-mounted sensors.

Features	Gyroscope	Accelerometer
Sampling rate	200 Hz	200 Hz
Dynamic range	1000°/s	16 g
Bias instability	12°/h	0.06 mg
White noise	18°/h$^{1/2}$	0.025 m·s^{-1}·h$^{-1/2}$

5.1. Performance evaluation of QSMF recognition

This study presents the Bi-LSTM algorithm for the detection of the QSMF period during pedestrian walking. The algorithm leverages feature extraction from MEMS sensors to improve the precision of the existing QSMF recognition approach. To train the algorithm, a dataset containing 60 trajectories with marked QSMF periods is collected. Additionally, a separate dataset of 20 trajectories is collected for accuracy evaluation. The detected QSMF periods are labeled and depicted in Fig. 4.

To assess the effectiveness of the developed QSMF detection algorithm, three state-of-the-art architectures are employed for comparison purposes. To ensure fairness, identical test trajectories are utilized for accuracy comparison. Two precision indices, namely the Time Accuracy (comparing the detected QSMF time period with

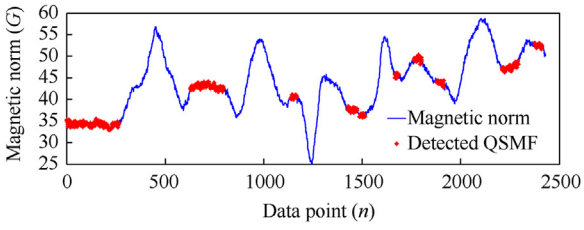

Fig. 4. Marked QSMF periods of selected trajectory.

Table 2
Accuracy indexes of QSMF recognition algorithms.

Models	Time index	Detection index
Thresholds [15]	68%	100%
1D-CNN [12]	76%	100%
LSTM [2]	89%	100%
Bi-LSTM	94%	100%

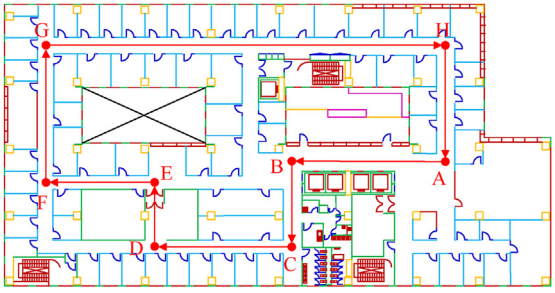

Fig. 5. Walking route in 8th floor.

the overall QSMF period) and the Detection Rate (comparing the recognized amount of QSMF events with the overall amount), are adopted for evaluation. The comparison description of four different QSMF recognition algorithms is presented as follows.

Table 2 showcases the superior performance of the presented Bi-LSTM algorithm compared with three other existing methods. All four models achieved the same detection index of 100%, and the Bi-LSTM algorithm demonstrated significantly higher time index at 94% compared with the others, the higher the time index, the higher the efficiency of QSMF detection.

Table 3
Walking Speed Estimation Errors Comparison using Different Models.

Indexes/Models	IONet	RONIN	WSP
Mean/(m·s^{-1})	0.058	0.053	**0.045**
Std/(m·s^{-1})	0.046	0.028	**0.026**
Max/(m·s^{-1})	0.163	0.129	**0.112**
Min/(m·s^{-1})	0.011	0.026	**0.013**
75th/(m·s^{-1})	0.085	0.071	**0.062**
Median/(m·s^{-1})	0.042	0.038	**0.033**

Table 4
Comparison Results using Different Datasets.

Datasets/Models	IONet/m	RONIN/m	WSP/m
RoNIN	1.71	1.66	**1.58**
OxIOD	1.83	1.79	**1.72**
ADVIO	2.01	1.93	**1.79**
Ours	1.82	1.74	**1.52**

To evaluate the positioning accuracy based on four different QSMF recognition approaches, we conducted experiments in a typical indoor office environment. A classical PDR [27] was employed as the baseline positioning model. The pedestrian began at point A and traversed points B, C, D, E, F, G, H, before returning to point A. The walking route is illustrated in Fig. 5. Fig. 6(a) portrays the calculated walking speed and attitude information, while

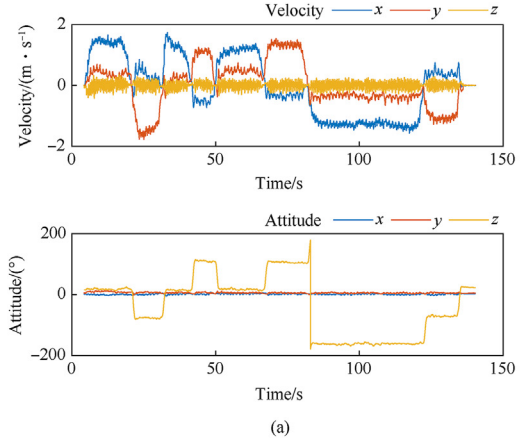

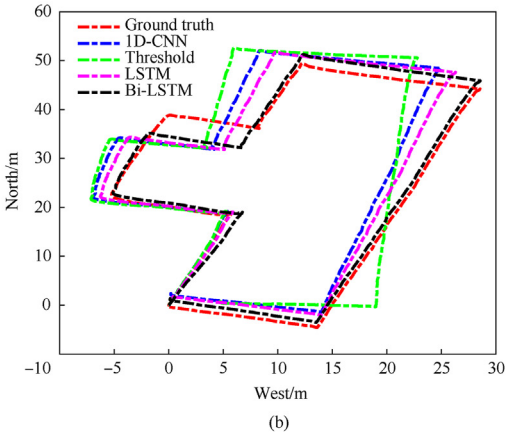

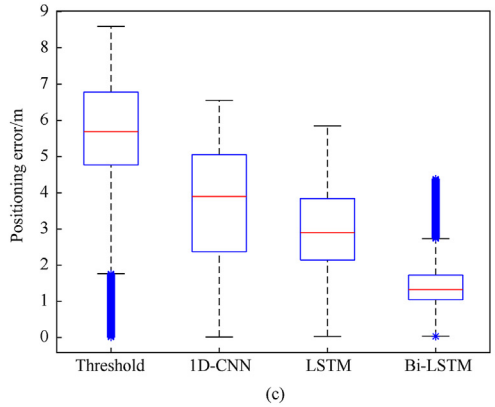

Fig. 6. (a) Speed and attitude calculation results; (b) Trajectories comparison between different models; (c) Positioning errors comparison between different models; (d) Dataset collection system [29].

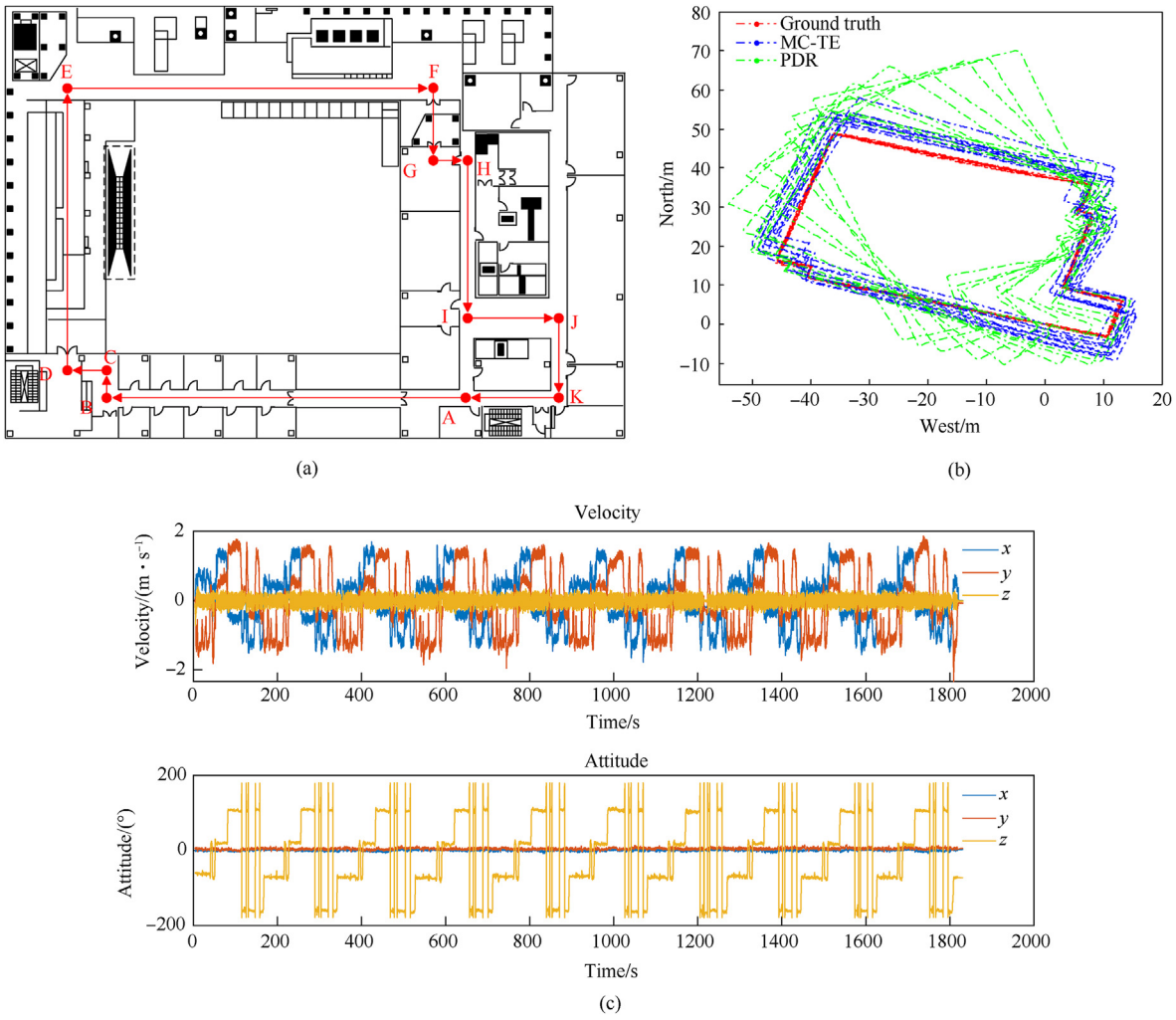

Fig. 7. (a) Long-term walking route; (b) Estimated trajectories between PDR and MC-TE; (c) Estimated velocity and attitude using MC-TE.

Figs. 6(b) and 6(c) compare the estimated trajectories and their respective accuracy using the four QSMF detection algorithms.

As illustrated in Figs. 6(b) and 6(c), the presented Bi-LSTM model demonstrates a notable enhancement in the overall localization performance by accurately detecting QSMF periods compared to the LSTM, 1D-CNN, and threshold-based approaches. The final evaluated localization error of the raw trajectory based on Bi-LSTM is below 1.72 m in 75% of cases, showcasing superior performance when compared to the LSTM approach (3.84 m in 75%), 1D-CNN (5.05 m in 75%), and threshold-based approach (6.78 m in 75%).

5.2. Performance evaluation of walking speed estimator

In this work, data-driven approach is proposed for walking speed estimation, by collecting various motion features for model training and prediction. To evaluate the effectiveness of the presented walking speed prediction (WSP) algorithm, we compare it with existing data-driven models: RONIN [31] and IONet [32]. For the training and test datasets generation, we use the Lidar-based SLAM system to provide centimeter-level location reference and related walking speed calculation results as the ground-truth value, in which the waist-mounted MEMS sensors module is also integrated into this system for dataset collection [11]. In the on-line phase, the collected sensors data are transmitted to smartphone for trajectory estimation. We utilize the same test dataset consists of 20 trajectories for comparison, the overall dataset collection system is shown in Fig. 6(d).

For the model training of proposed Bi-LSTM-based WSP, the transformed IMU data and extracted motion features are modelled as the input vector for Bi-LSTM network training purposes. We choose the learning rate as 1e-5, epoch as 1000, loss function as "mse", and optimizer as "adam" to get the optimal Bi-LSTM network model, and then use the test dataset for accuracy comparison with existing networks. The comparison results are described in Table 3.

Table 3 indicates that the proposed WSP model realizes the better speed estimation accuracy compared with other two existing models including RONIN and IONet, the estimated speed estimation error is lower than 0.062 m/s in 75% cumulated percentage, and the estimated mean error is lower than 0.045 m/s.

In addition, we also compared the positioning performance of proposed WSP model using different open-source datasets including: RoNIN [31], OxIOD [33], ADVIO [34], and ours. In this case, we use the heading information provided by hybrid heading estimation method proposed in Ref. [35], and then we compare the mean error of updated trajectory location provided by three different trajectory update algorithms in Table 4.

It can be found from Table 4 that the proposed WPS in this work proves the best trajectory update performance under four different

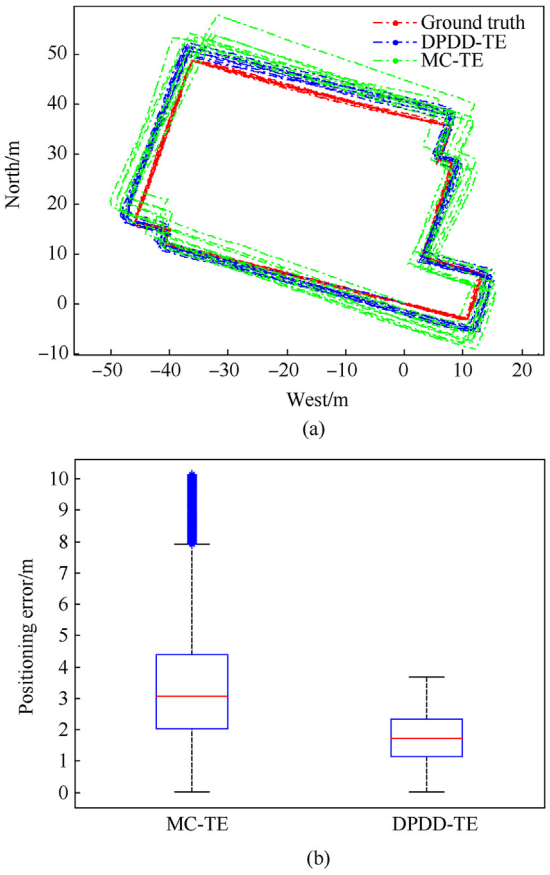

Fig. 8. (a)Estimated trajectories between MC-TE and DPDD-TE; (b) Estimated errors between MC-TE and DPDD-TE.

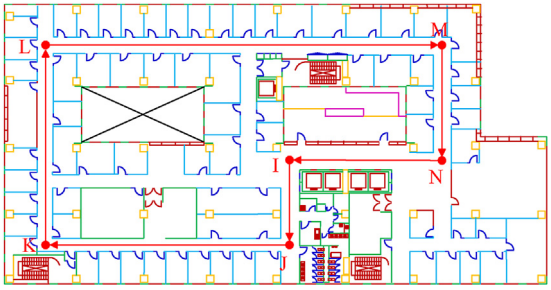

Fig. 9. Walking route in 9th floor.

datasets. The estimated mean errors of updated trajectory location of proposed WSP under four datasets are 1.58 m, 1.72 m, 1.79 m, 1.52 m, respectively.

5.3. Performance evaluation of multi-level constraints based localization

The present study introduces the multi-level constraints-based trajectory estimator (MC-TE) as a solution to mitigate the divergence and cumulative deviations stemming from the INS algorithm. In this approach, ZUPT and NHC are employed to enforce velocity constraints, while the ZARU and QSMF are utilized to enforce heading constraints. A long-term walking route is conducted for performance evaluation, the testers started from the point A, walked through the points B—K, and back to the point A, the overall

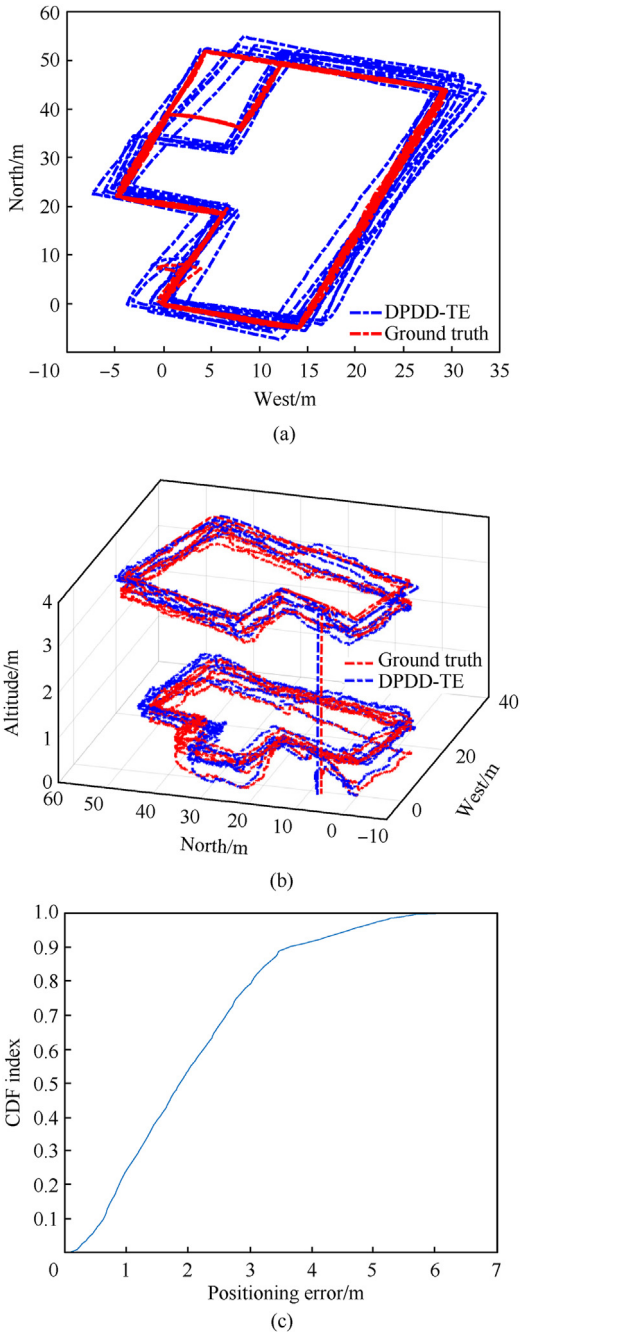

Fig. 10. (a) Estimated 2D trajectory of DPDD-TE; (b) Estimated 3D trajectory of DPDD-TE; (c) Positioning error proposed DPDD-TE.

Table 5
The execution time (ms) under different terminals.

Method	Pixel 4	Pixel 5	Pixel 6	Huawei P30
DPDD-TE	15.28	13.74	11.24	12.63

route is repeated 10 rounds, with a time duration of more than 30 min. The performance comparison between classical PDR [27] and developed MC-TE is described in Fig. 7(b), and the velocity and attitude estimation results of MC-TE are shown in Fig. 7(c).

Figs. 7(b) and 7(c) indicate that the integration of multi-level constraints and observations effectively decrease the cumulative

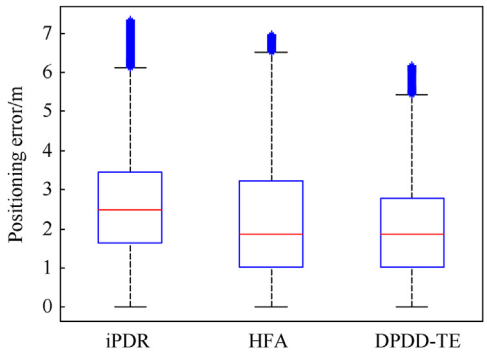

Fig. 11. Performance comparison using different structures.

error of single INS update method, and realizes the much higher positioning and attitude estimation accuracy, in which the localization error is lower than 4.39 m in 75%, and the heading estimation error is less than 5° after 30 min uses.

5.4. Experiment results of DPDD-TE algorithm

This paper proposes the DPDD-TE algorithm contains the loop detection algorithm using detected magnetic and trajectory features, and the positioning performance can be further enhanced when there are loop points detected among the testers' walking route. For the walking route described in Fig. 7(a), the RTS algorithm is applied for trajectory optimization after loop detection procedure. The comparison between trajectories provided by MC-TE and final DPDD-TE is compared in Figs. 8(a) and 8(b).

Figs. 8(a) and 8(b) indicate that the developed DPDD-TE realizes much higher positioning accuracy compared with MC-TE with the assistance of loop detection and RTS based trajectory optimization. The final estimated positioning error decreases from 4.39 m in 75% to 2.36 m in 75%.

To evaluate the performance of presented DPDD-TE structure in complex 3D environments, two adjacent floors in a large office building are adopted for experimental purposes, the tester repeated the walking route A-H-A for 7 times, go upstairs, I–N–I for 7 times, go downstairs, and returned to the point N, with an overall duration of more than 30 min. The overall walking route is compared in Figs. 5 and 9. The calculated 2D and 3D trajectory by the proposed DPDD-TE is described in Fig. 10.

Fig. 10 represents that the presented DPDD-TE framework with multi-level constraints and loop detection effectively enhance the localization precision under complex 3D indoor environments. The final estimated localization error is less than 2.79 m in 75%. We also compare the computational efficiency and real-time performance of proposed DPDD-TE under different mobile terminals, the comparison results are described in Table 5.

It can be found from Table 5 that the proposed DPDD-TE in this paper realizes high efficiency and real-time performance under different mobile platform, that can realizes the output rate of higher than 50 Hz.

Finally, the precision of presented DPDD-TE is compared with state-of-art integrated INS-PDR framework (iPDR) [15] and histogram feature-based approach (HFA) [36] with the same heading information provided by DPDD-TE. To be fair, the same walking route presented in Figs. 5 and 9 is adopted, and the estimated localization errors of proposed DPDD-TE, iPDR and HFA are compared in Fig. 11.

Fig. 11 indicates that the developed DPDD-TE realizes significant beyond performance than iPDR and HFA algorithms under the same test conditions and environments, and the realized localization errors of three structures are 2.75 m in 75% (DPDD-TE), 3.33 m in 75% (iPDR), and 3.23 m in 75% (HFA), respectively, and the average localization error of proposed DPDD-TE is less than 2 m.

6. Conclusions

In order to increase the performance of indoor positioning using waist-mounted devices across multiple floors, this study presents the DPDD-TE framework, which encompasses four main contributions:

1) An innovative Bi-LSTM is applied to enhance interference detection of the local magnetic field. Real-time features from inertial sensors and magnetometers are modelled and used as input vectors for training and prediction purposes. The recognized QSMF periods are further modelled as magnetic observations for heading calibration.
2) A Bi-LSTM network-based model for predicting walking speeds is introduced. This model takes into account raw data and motion features provided by waist-mounted inertial sensors, resulting in more accurate walking speed information compared to traditional approaches.
3) Multi-level observables are proposed for tracking instances of the QSMF, step length, and location increments. Additionally, multi-level constraints such as ZUPT/ZARU, altitude constraints, and NHC are introduced. These observations and constraints are combined with INS mechanization to decrease the impact of divergence and cumulative errors, magnetic interference, and external accelerations originating from the built-in sensors.
4) Based on estimation results from QSMF detection, walking speed estimation, and hybrid observations, the DPDD-TE framework is proposed. It employs a unified Unscented Kalman filter (UKF) that combines the INS mechanization with the aforementioned observations and constraints. This approach is further enhanced by a loop detection algorithm that utilizes magnetic and trajectory features. The integration of multiple models effectively improves the accuracy and stability of presented DPDD-TE localization system.

In general, the proposed DPDD-TE framework provides a comprehensive solution for accurate 3D indoor positioning and optimization using waist-mounted devices. Experimental results demonstrate that DPDD-TE achieves significantly higher long-term positioning accuracy compared to state-of-the-art algorithms. For the effects of various scenarios and motion modes, the constraints and observations like ZUPT/ZARU, PDR, Gravity vector, QSMF, and pressure/stair observation are modelled regardless of exercise situations and modes, and the NHC, SL constraint, Bi-LSTM-based WSP is applied to improve the walking speed estimation accuracy under the case of walking forward in our work. Under the other cases such as walking backwards or lateral walking, the motion mode detection algorithm is also required for the assistance of walking speed estimation of Bi-LSTM-based WSP, this is also our future work.

Declaration of competing interest

The authors declare that they have no known competing financial interests or personal relationships that could have appeared to influence the work reported in this paper.

References

[1] Yu Y, Chen R, Chen L, et al. H-WPS: hybrid wireless positioning system using an enhanced wi-fi FTM/RSSI/MEMS sensors integration approach. IEEE

Internet Things J 2021;9(14):11827–42.
[2] Liu Z, Shi W, Yu Y, et al. A LSTM-based approach for modelling the movement uncertainty of indoor trajectories with mobile sensing data. Int J Appl Earth Obs Geoinf 2022;108:102758.
[3] Munzert S, Selb P, Gohdes A, et al. Tracking and promoting the usage of a COVID-19 contact tracing app. Nat Human Behav 2021;5(2):247–55.
[4] Yu Y, Chen R, Chen L, et al. A robust seamless localization framework based on Wi-Fi FTM/GNSS and built-in sensors. IEEE Commun Lett 2021;25(7):2226–30.
[5] Zhuang Y, Zhang C, Huai J, et al. Bluetooth localization technology: Principles, applications, and future trends. IEEE Internet Things J 2022;9(23):23506–24.
[6] Ridolfi M, Kaya A, Berkvens R, et al. Self-calibration and collaborative localization for UWB positioning systems: a survey and future research directions. ACM Comput Surv 2021;54(4):1–27.
[7] Ruan Y, Chen L, Zhou X, et al. iPos-5G: indoor positioning via commercial 5G NR CSI. IEEE Internet Things J 2022;10(10):8718–33.
[8] Yu Y, Shi W, Chen R, et al. Map-assisted seamless localization using crowdsourced trajectories data and Bi-LSTM based quality control criteria. IEEE Sensor J 2022;22(16):16481–91.
[9] Chen R, Li Z, Ye F, et al. Precise indoor positioning based on acoustic ranging in smartphone. IEEE Trans Instrum Meas 2021;70:1–12.
[10] Kuang J, Li T, Chen Q, et al. Consumer-grade inertial measurement units enhanced indoor magnetic field matching positioning scheme. IEEE Trans Instrum Meas 2022;72:1–14.
[11] Bao S, Shi W, Chen P, et al. A systematic mapping framework for backpack mobile mapping system in common monotonous environments. Measurement 2022;197:111243.
[12] Qi L, Yu Y, Liu Y, et al. A robust foot-mounted positioning system based on dual IMU data and ultrasonic ranging. IEEE Sensor J 2023;23(4):4085–95.
[13] Qi L, Liu Y, Gao C, et al. Hybrid pedestrian positioning system using wearable inertial sensors and ultrasonic ranging. Defence Technology 2023;33:327–38.
[14] Li Z, Jiang C, Gu X, et al. Collaborative positioning for swarms: a brief survey of vision, LiDAR and wireless sensors based methods. Defence Technology 2024;33:475–93.
[15] Kuang J, Niu X, Chen X. Robust pedestrian dead reckoning based on MEMS-IMU for smartphones. Sensors 2018;18(5):1391.
[16] Liu T, Kuang J, Ge W, et al. A simple positioning system for large-scale indoor patrol inspection using foot-mounted INS, QR code control points, and smartphone. IEEE Sensor J 2020;21(4):4938–48.
[17] Wan Q, Duan X, Yu Y, et al. Self-calibrated multi-floor localization based on wi-fi ranging/crowdsourced fingerprinting and low-cost sensors. Rem Sens 2022;14(21):5376.
[18] Kuang J, Li T, Niu X. Magnetometer bias insensitive magnetic field matching based on pedestrian dead reckoning for smartphone indoor positioning. IEEE Sensor J 2021;22(6):4790–9.
[19] Lawal IA, Bano S. Deep human activity recognition using wearable sensors[C]. In: Proceedings of the 12th ACM International Conference on PErvasive technologies related to assistive environments; 2019. p. 45–8.
[20] Yu N, Li Y, Ma X, et al. Comparison of pedestrian tracking methods based on foot-and waist-mounted inertial sensors and handheld smartphones. IEEE Sensor J 2019;19(18):8160–73.
[21] Li Y, Zhuang Y, Zhang P, et al. An improved inertial/wifi/magnetic fusion structure for indoor navigation. Inf Fusion 2017;34:101–19.
[22] Foxlin E. Pedestrian tracking with shoe-mounted inertial sensors. IEEE Computer graphics and applications 2005;25(6):38–46.
[23] Tong X, Su Y, et al. A double-step unscented Kalman filter and HMM-based ZeroVelocity update for pedestrian dead reckoning using MEMS sensors. IEEE Trans Ind Electron 2019;67(1):581–91.
[24] Li Y, Georgy J, Niu X, et al. Autonomous calibration of MEMS gyros in consumer portable devices. IEEE Sensor J 2015;15(7):4062–72.
[25] Wang Q, Fu M, Wang J, et al. Free-walking: pedestrian inertial navigation based on dual foot-mounted IMU. Defence Technology 2024;33:573–87.
[26] Jouybari A, Ardalan AA, Rezvani MH. Experimental comparison between Mahoney and Complementary sensor fusion algorithm for attitude determination by raw sensor data of Xsens IMU on buoy. Int Arch Photogram Rem Sens Spatial Inf Sci 2017;42:497–502.
[27] Yu Y, Chen R, Chen L, et al. Autonomous 3D indoor localization based on crowdsourced Wi-Fi fingerprinting and MEMS sensors. IEEE Sensor J 2021;22(6):5248–59.
[28] Zhang L, Cheng M, Xiao Z, et al. Adaptable map matching using PF-net for pedestrian indoor localization. IEEE Commun Lett 2020;24(7):1437–40.
[29] Yu Y, Yao Y, Liu Z, et al. A Bi-LSTM approach for modelling movement uncertainty of crowdsourced human trajectories under complex urban environments. Int J Appl Earth Obs Geoinf 2023;122:103412.
[30] Wu Y, Chen R, Li W, et al. Indoor positioning based on walking-surveyed Wi-Fi fingerprint and corner reference trajectory-geomagnetic database. IEEE Sensor J 2021;21(17):18964–77.
[31] Herath S, Yan H, Furukawa Y. Ronin: robust neural inertial navigation in the wild: Benchmark, evaluations, & new methods[C]//2020. IEEE International Conference on Robotics and Automation (ICRA). IEEE 2020:3146–52.
[32] Chen C, Lu X, Markham A, et al. Ionet: learning to cure the curse of drift in inertial odometry[C]. Proc AAAI Conf Artif Intell 2018;32(1).
[33] Chen C, Zhao P, Lu CX, et al. Deep-learning-based pedestrian inertial navigation: methods, data set, and on-device inference. IEEE Internet Things J 2020;7(5):4431–41.
[34] Cortés S, Solin A, Rahtu E, et al. ADVIO: an authentic dataset for visual-inertial odometry[C]. In: Proceedings of the European Conference on computer Vision. ECCV); 2018. p. 419–34.
[35] Li W, Chen R, Yu Y, et al. Pedestrian dead reckoning with novel heading estimation under magnetic interference and multiple smartphone postures. Measurement 2021;182:109610.
[36] Pham TT, Suh YS. Histogram feature-based approach for walking distance estimation using a waist-mounted IMU. IEEE Sensor J 2020;20(20):12354–63.